International Journal of Particle Therapy 11 (2024) 100013

Contents lists available at ScienceDirect

International Journal of Particle Therapy

journal homepage: www.sciencedirect.com/journal/ijpt

Dosimetric Evaluation of Target Motion Effects in Spot-Scanning Proton Therapy: A Phantom Study

Mikhail Belikhin (PhD)[1,2,*], Alexander Shemyakov (MS)[1], Alexander Chernyaev (PhD, ScD)[2], Alexander Pryanichnikov (PhD)[3,**]

[1] JSC Protom, Protvino, Russian Federation
[2] Lomonosov Moscow State University, Moscow, Russian Federation
[3] Division of Biomedical Physics in Radiation Oncology, German Cancer Research Center (DKFZ), Heidelberg, Germany

ARTICLE INFO

Keywords:
Spot-scanning proton therapy
Intrafractional target motion
Dynamic phantom
Dosimetry
Interplay effect

ABSTRACT

Purpose: To evaluate intrafractional motion effects as a function of peak-to-peak motion and period during single-field, single-fraction and single-field, multifraction irradiation of the moving target in spot-scanning proton therapy.

Materials and Methods: An in-house dynamic phantom was used to simulate peak-to-peak motion of 5, 10, and 20 mm with periods of 2, 4, and 8 seconds. The dose distribution in the moving target was measured using radiochromic films. During the perpendicular motion, the film was fixed and moved perpendicular to the beam direction without changing the water equivalent thickness (WET). During longitudinal motion, the film was fixed and moved along the beam direction, causing a change in WET. Gamma index analysis was used with criteria of 3%/3 mm and 3%/2 mm to analyze the dose distributions.

Results: For single-fraction irradiation, varying the period did not result in a significant difference in any of the metrics used ($P > .05$), except for the local dose within the planning target volume ($P < .001$). In contrast, varying peak-to-peak motion was significant ($P < .001$) for all metrics except for the mean planning target volume dose ($P \approx .88$) and the local dose ($P \approx .47$). The perpendicular motion caused a greater decrease in gamma passing rate (3%/3 mm) than WET variations (65% ± 5% vs 85% ± 4%) at 20 mm peak-to-peak motion.

Conclusion: The implementation of multifraction irradiation allowed to reduce hot and cold spots but did not reduce dose blurring. The motion threshold varied from 7 to 11 mm and depended on the number of fractions, the type of motion, the acceptance criteria, and the calculation method used.

Introduction

Pencil beam proton therapy has the potential to reduce acute normal tissue toxicity compared to conventional photon radiotherapy in the treatment of lung, breast, and liver. However, intrafractional tumor motion[1] results in clinically significant dose distortion due to blur, interplay, and range effects. The blur effect is caused by target motion perpendicular to the beam direction and is manifested as dose blur along the direction of motion. The interplay effect causes localized overdosage and underdosage spots due to target motion relative to the beam scan setting. The range effect manifests as Bragg peak shifts when there are anatomical variations in water equivalent thickness (WET).

Previous studies have mostly investigated the motion effects using four-dimensional (4D) calculations based on 4D computed tomography (4DCT) data sets.[2-8] Experimental evaluation has been performed using 4D phantoms, radiochromic films, and 2-dimensional (2D) ion chamber (IC) array detectors.[9-11] Intrafractional tumor motion limits the ability to use free-breathing irradiation and cannot be compensated by the margin around the tumor,[2] requiring the advanced motion mitigation techniques recommended in the AAPM TG-290 report.[12] The motion threshold for active motion mitigation varies between studies from 4[13] to 10 mm[10] and depends on the specific delivery system[3] and the number of irradiation fields and fractions.[6]

* Corresponding author. JSC Protom, Protvino 142281, Russian Federation.
** Corresponding author. Division of Biomedical Physics in Radiation Oncology, German Cancer Research Center (DKFZ), Heidelberg 69120, Germany.
E-mail addresses: mikhailbelikhin@protom.ru (M. Belikhin), alexander.pryanichnikov@dkfz-heidelberg.de (A. Pryanichnikov).

https://doi.org/10.1016/j.ijpt.2024.100013
Received 17 November 2023; Received in revised form 15 March 2024; Accepted 18 March 2024
2331-5180/© 2024 The Author(s). Published by Elsevier B.V. on behalf of Particle Therapy Co-operative Group. This is an open access article under the CC BY-NC-ND license (http://creativecommons.org/licenses/by-nc-nd/4.0/).

In the present study, motion effects during single-field, single-fraction and single-field, multifraction spot-scanning proton therapy were dosimetrically evaluated as a function of peak-to-peak motion and period using a dynamic phantom and radiochromic films. The results were used to define the facility-specific motion threshold for active motion mitigation.

Materials and methods

Proton therapy facility

The present study was performed at the proton therapy complex Prometheus (JSC Protom, Protvino, Russian Federation) located at the Protvino city hospital.[14,15] It is a commercially available synchrotron-based system for intensity-modulated proton therapy with a spot-scanning beam delivery technique. The Prometheus contains a gantry-less beam delivery system with a horizontal beam specified for upright patient position.[16] The synchrotron provides a narrow scanning beam with an intensity of approximately 10^9 protons per cycle in the energy range of 30 to 330 MeV, which is suitable for both treatment[17] and proton imaging.[18] An energy switch time varies in the range of 1.2 to 1.5 seconds; a spot switch time is typically 5 ms. The beam size (σ) is 9.1 to 1.7 mm for the beam energy of 40 to 250 MeV. This synchrotron has also been integrated into other commercially available proton therapy systems, including the Radiance 330 proton therapy system (ProTom International Holding Corporation)[19] and the P-Cure proton therapy system (P-Cure Ltd, Shilat, Israel).[20]

Dynamic phantom and dosimetry

An in-house dynamic water phantom[21] was used to simulate intrafractional target motion. The phantom (Figure 1a) consisted of a plexiglass container filled with water and a plastic target attached to a servo. Radiochromic films EBT3 (Ashland, Oregon) cut to 100 mm × 92 mm size were installed in the central slot of the target as shown in Figure 1 to measure the 2D dose distribution. The target had side windows for unobstructed beam delivery so that only water was in the beam path. The irradiated films were scanned with an Epson V700 (Epson, Tokyo, Japan) at a resolution of 72 dots per inch in landscape orientation 24 hours after irradiation. The film's images were converted into dose matrices using the 3-order polynomial calibration performed on a ^{60}Co source[22] in the dose range of 0.1 to 15.0 Gy using the red color channel. The phantom was positioned according to preapplied marks on its body (Figure 1a) using laser pointers integrated into the treatment room. Position alignment was also performed immediately prior to irradiation using a built-in X-ray system.

Motion patterns

The phantom moved the film along a single direction with triangular patterns (Figure 1d). These patterns provided regular target motion ranging from 5 to 20 mm (peak-to-peak) with a constant cycle period ranging from 2 to 8 seconds. The simulated target motion was similar to the respiration-induced motion and included 2 phases: the inhalation phase and the exhalation phase, which was longer than the inhalation phase. In particular, the exhalation phase contained 2 states: a dynamic state when the target was moving and a pause when the target was stationary. The triangular patterns used were asymmetric with respect to the mean line. The asymmetric pattern is more similar to the breathing patterns of most real patients and may introduce a dosimetric effect in multifraction irradiation[11] compared to the most commonly used sinusoidal wave pattern. In summary, a total of 9 triangular motion patterns with different motion ranges and periods were used in the current study (peak-to-peak motion—period): 5 mm—2 seconds, 10 mm—2 seconds, 20 mm—2 seconds, 5 mm—4 seconds, 10 mm—4 seconds, 20 mm—4 seconds, 5 mm—8 seconds, 10 mm—8 seconds, and 20 mm—8 seconds. The exhalation phase occupied approximately 63% of the movement cycle for all patterns used, and the pause state was 18% to 43% of the exhalation phase for motion periods of 2 to 8 seconds

In addition, 2 types of target motion were provided: perpendicular motion and longitudinal motion. During perpendicular motion (Figure 1b), the film was set and moved perpendicular to the beam direction, and the water thickness between the nozzle and the moving film did not change. During longitudinal motion (Figure 1c), the film was set and moved along the beam direction without perpendicular shifts, causing a change in water thickness equivalent to WET variations in real patient anatomy.

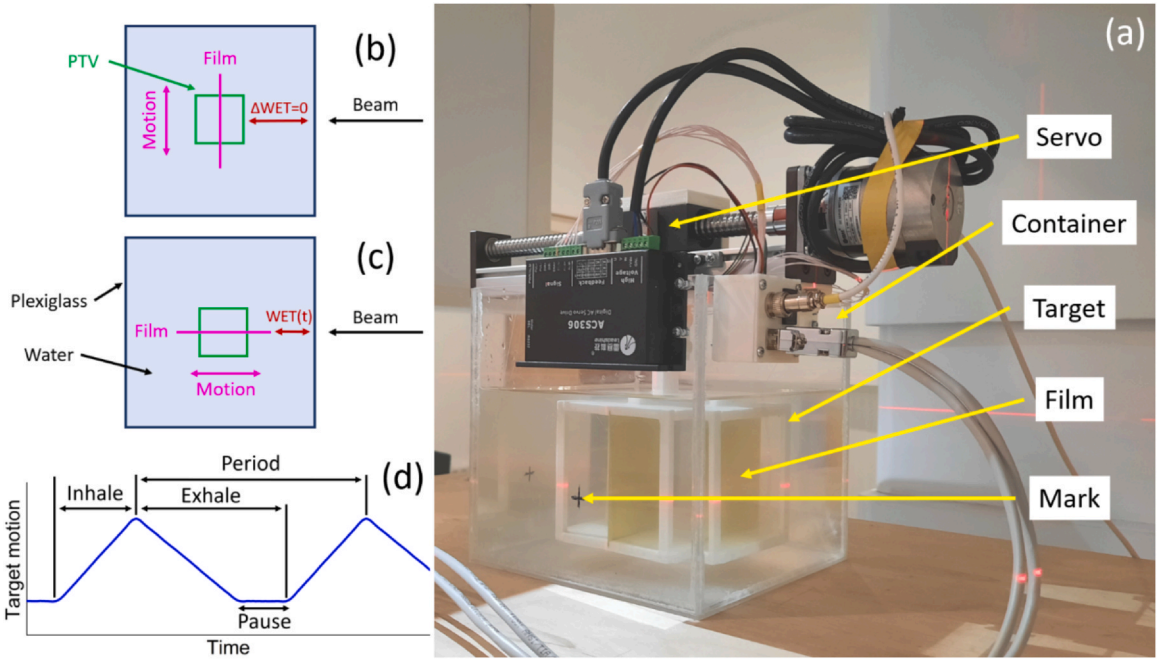

Figure 1. (a) The setup for simulating (b) perpendicular and (c) longitudinal motion (top view) with the dynamic phantom and (d) the triangular motion pattern diagram. Abbreviations: PTV, planning target volume; WET, water equivalent thickness.

Planning and irradiation

The current study included single-field, single-fraction and single-field, multifraction irradiations of the stationary and moving target. A cube-shaped planning target volume (PTV) with a size of 5 cm × 5 cm × 5 cm was centered in the phantom (Figure 1b) so that the film moved in water relative to the stationary PTV. Three irradiation plans were calculated using a Monte-Carlo-based treatment planning system integrated with the Prometheus software. A voxel size of 1 mm × 1 mm × 1 mm was selected in the treatment planning system. There were 33 energy slices in all calculated plans, with beam energy ranging from 101 to 133 MeV and beam size (σ) ranging from 3.7 to 3.1 mm.

Validation of the calculated plans was performed using a PinPoint 31022 IC (PTW, Freiburg, Germany). The dose was measured at the central point of the PTV and 6 points 2 cm from the central point in 6 orthogonal directions. The discrepancy between calculated and measured doses was within 3% for all points. In addition, the dose distributions were measured 3 times in the stationary target using the EBT3 films placed in perpendicular and longitudinal orientations relative to the nozzle of the beam delivery system (Figure 1b and c).

For single-fraction irradiation, the plan was calculated with a prescribed dose of 1.5 Gy. Irradiation of the moving target was performed using all 9 motion patterns described above for perpendicular motion and only 3 patterns of 5 mm—4 seconds, 10 mm—4 seconds, and 20 mm—4 seconds for longitudinal motion. Beam delivery was started randomly relative to the target motion phase. For all motion patterns used, the dose distribution measurement with EBT3 was repeated 3 times to calculate statistical variance. In total, 36 single-fraction irradiation sessions and measurements were performed. The average beam delivery time was 1 min 34 s.

For multifraction irradiation, 2 plans were calculated with a prescribed dose of 15 Gy and with 10 and 30 fractions. Irradiation of the moving target was performed for perpendicular and longitudinal motion using 3 motion patterns of 5 mm—4 seconds, 10 mm—4 seconds, and 20 mm—4 seconds. An irradiation session represented many fractions which were delivered sequentially one after another, starting from a random phase of target motion. The dose distribution was measured once with EBT3 for each motion pattern used. As a result, 12 multifraction irradiation sessions and measurements were performed. The average beam delivery time per fraction was 1 min 34 s and 1 min 1 s for the 10-fraction and 30-fraction plans, respectively. The total irradiation session time was approximately 20 and 45 minutes for the 10-fraction and 30-fraction plans, respectively.

Data analysis

The dose distributions acquired with EBT3 films were represented as 2D dose matrices and analyzed using in-house software developed in LabWindows/CVI (National Instruments, Austin, Texas). Two regions of interest (ROI) were delineated for quantitative analysis (Figure 2). The ROIs were rectangular in shape and bounded by pixels with coordinates $(i_1;j_1)$, $(i_1;j_2)$, $(i_2;j_1)$, and $(i_2;j_2)$, as shown in Figure 2a. ROI1 had a size of 50 mm × 50 mm and followed the PTV contour. For the perpendicular orientation of the film, ROI2 consisted of 2 areas of 50 mm × 15 mm, symmetrically adjacent to ROI1 on either side (Figure 2a). For the longitudinal orientation, only 1 area of 50 mm × 15 mm was delineated (Figure 2b). ROI2 was used to evaluate dose distribution beyond the PTV. In addition, 1 pixel was randomly selected within ROI1 to estimate local dose variations.

All dose distributions obtained in the moving target were normalized to the mean dose in ROI1 in the stationary target. Several metrics were used to analyze the dose distributions, including mean dose (D_m) in ROI1 and ROI2, dose inhomogeneity (*IH*) in ROI1, and gamma passing rate (GPR) in gamma index analysis. In addition, 1-way analysis of variance with a significance level of $P < .05$ was applied to statistically compare the dose distributions obtained for different motion patterns. The inhomogeneity quantified the degradation of dose homogeneity in the moving target (H_{mov}) due to the motion effects relative to that in the stationary target (H_{st}) and was calculated using Equation 1:

$$IH = H_{st} - H_{mov} \tag{1}$$

Homogeneity was calculated using a root-mean-square analysis of the dose distribution at the pixel level, expressed as Equation 2:

$$H_{st},\, H_{mov} = 100\% - \frac{1}{D_m}\sqrt{\frac{\sum_{i=i_1,j=j_1}^{i_2,j_2}(D_{ij} - D_m)^2}{(i_2 - i_1)(j_2 - j_1)}} \cdot 100\% \tag{2}$$

where D_{ij} is the dose in the pixel with coordinates $(i;j)$. This approach was similar to that previously proposed by Bert et al,[9] allowing for a direct comparison between the results of our study and Bert's study.

Gamma index analysis with 2 acceptance criteria of 3%/3 mm and 3%/2 mm was used to quantify the dose distributions measured in the moving target. For both criteria, the local gamma index and the global gamma index, normalized to the mean stationary dose in ROI1, were calculated using a 10% low-dose threshold (LDT) relative to the mean stationary dose in ROI1. The GPR thresholds of 95% and 90% were used for the 3%/3 mm and 3%/2 mm acceptance criteria, respectively. The 95% threshold is commonly used in clinical practice, and the 90% threshold was chosen based on the action limits recommended in the AAPM TG-218 report.[23]

In addition to the statistical variance of all metrics used, calculated based on multiple irradiations, uncertainties associated with the measurement of absolute dose using the EBT3 films were considered in the dose analysis. These uncertainties included the quenching effect,[24] calibration errors, darkening over time, and positioning errors of the film in the phantom. The quenching effect is an under-response of the dose at the peak of the Bragg curve, which can be up to 20% when the film is placed parallel to the central axis of the beam, as reported by Zhao

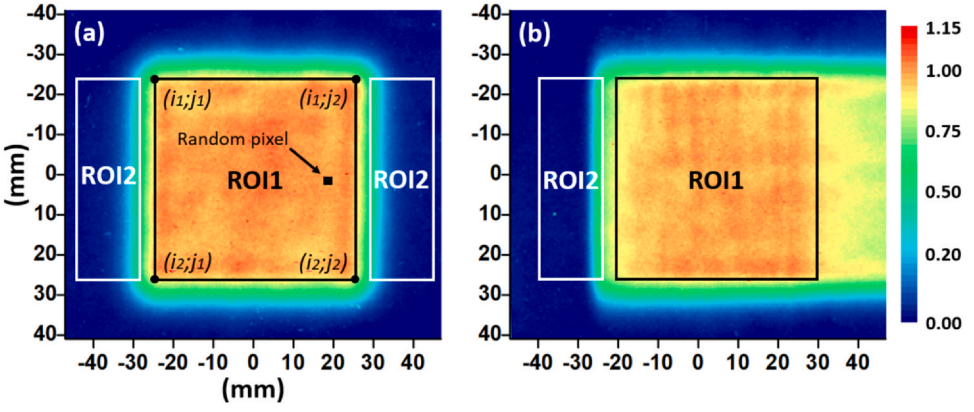

Figure 2. An example of the dose distributions obtained in the stationary target with 2 film orientations: (a) perpendicular (beam eye view, Figure 1b) and (b) longitudinal (side view, Figure 1c). The random pixel and the regions of interest that were located in the same way for the moving target are shown. Dose distributions were normalized to the mean dose in ROI1. Abbreviation: ROI, regions of interest.

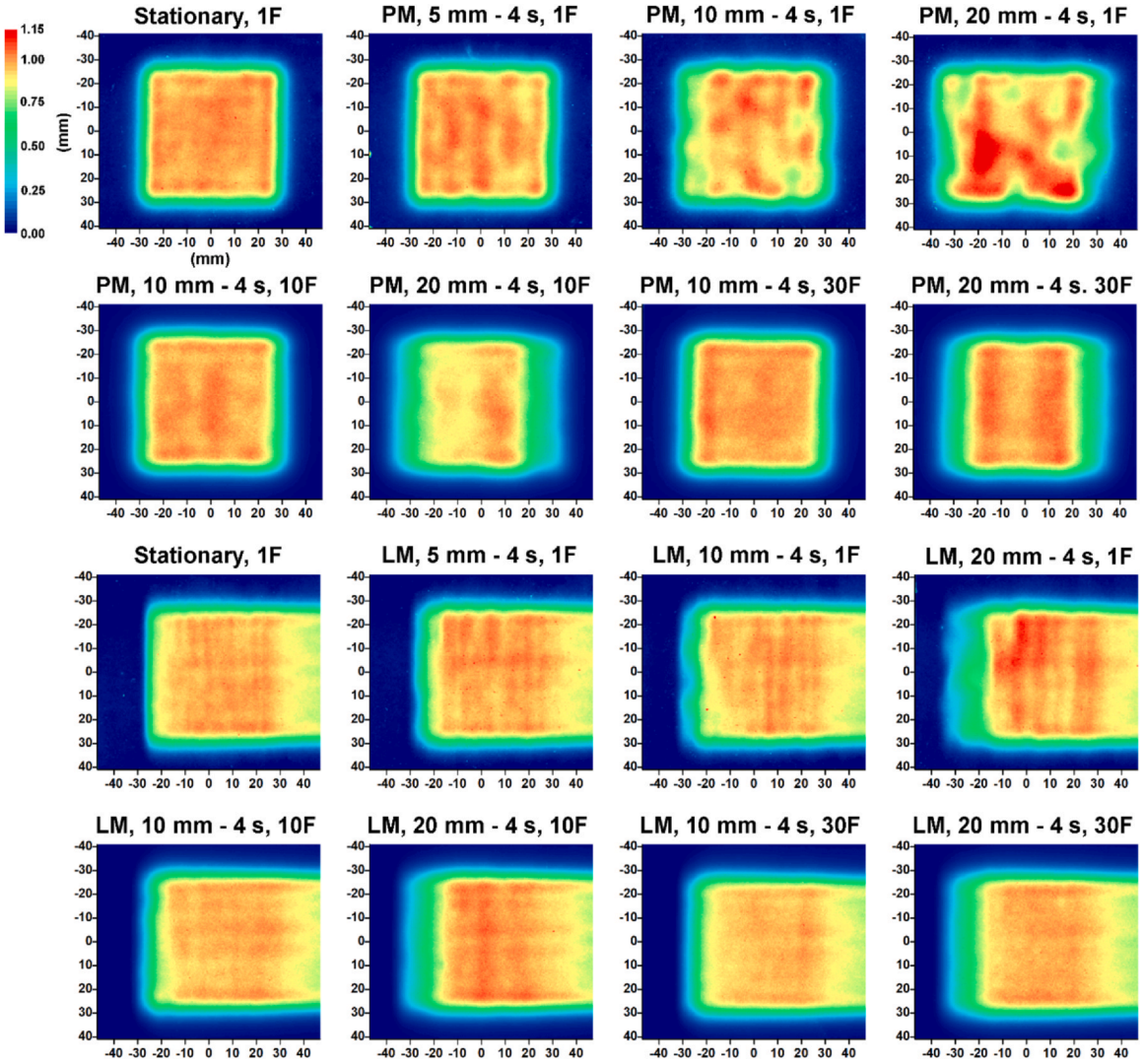

Figure 3. An example of dose distributions in the stationary target and the moving target irradiated with 1 fraction (1F), 10 fractions (10F), and 30 fractions (30F) at 5 mm—4 seconds, 10 mm—4 seconds, and 20 mm—4 seconds motion patterns during perpendicular motion (beam eye view) and longitudinal motion (side view, beam delivered from the right). Abbreviations: LM, longitudinal motion; PM, perpendicular motion.

et al.[25] This effect is observed in Figure 2b as a decrease in dose on the left side of ROI1, where the dose was predominantly delivered at the Bragg peak. At the same time, the planned dose distribution was more uniform, as confirmed by the IC validation described above. The calibration error was defined as the discrepancy between the dose measured by the IC during the calibration procedure and the dose obtained with the film by recalculation with a fitted polynomial equation. The discrepancy was found to be 3.2% (SD) and varied from −4.7% to +6.8% in the dose range of 0.2 to 15.0 Gy. Film positioning errors were related to film offsets within the slot of the target and uneven film edges during cutting, which introduced a non-negligible uncertainty in the metrics used. Although the phantom target had a side stop that allowed each film to be placed in approximately the same position, the positioning error was estimated to be ± 1 mm (range). Film positioning errors cannot be compensated for by alignment procedures that are related to the phantom body and not the film inserted into the target.

In the gamma index analysis, the dose distributions measured with EBT3 film in the stationary target were used as the reference for calculating the gamma index for the distribution in the moving target, rather than the planned distribution, which is the most commonly used.[26] This approach allowed a relative comparison of the dose distribution in the moving target, distorted by motion effects, and the planned distribution, thus reducing the uncertainty associated with the measurement of absolute dose using EBT3 films. To calculate the statistical variation of the GPR for the stationary dose distribution, the stationary distributions were compared with each other.

Homogeneity and GPR experimental data as a function of peak-to-peak target motion were fitted by a quadratic model, as suggested by Protik et al.[8] From the fitted data curve, the peak-to-peak motion corresponding to the GPR and H thresholds was calculated to determine the motion threshold. The GPR threshold was set at 95% and 90% for the 3%/3 mm and 3%/2 mm criteria, respectively, and the H threshold was set at 95%. Motion threshold was evaluated for perpendicular and longitudinal motion and 1, 10, and 30 fractions of irradiation.

Results

The acquired dose distributions are shown as color maps in Figure 3. When the moving target was irradiated in a single fraction, dose distortion was manifested as hot and cold spots and blurring along the direction of motion. Hot and cold spots were more acute for perpendicular motion than for longitudinal motion. At the same time, dose blurring along the direction of motion was observed for both types of motion. The implementation of multifraction irradiation allowed to mitigate hot and cold spots to some extent but did not reduce dose blurring. For 10 mm peak-to-peak motion, multifraction irradiation of

Table
Summary of quantitative results, including motion thresholds (MT_{GPR}) based on GPR, for dose distributions in the moving target irradiated with different numbers of fractions (N) at perpendicular motion and longitudinal motion.

N	Motion type	Period (s)	Motion pk-pk (mm)	D_m in ROI2	IH (%)	GPR (%)				MT_{GPR} (mm)
						3%/3 mm		3%/2 mm		
						Global	Local	Global	Local	
1	Stationary	NA[a]	NA	1.00 ± 0.10	0.0 ± 0.1	99.2 ± 0.4		98.0 ± 0.6		NA
1	PM	2	5	1.11 ± 0.21	2.1 ± 0.4	90.2 ± 2.5	90.1 ± 2.6	85.5 ± 2.6	85.2 ± 2.5	3
			10	1.44 ± 0.49	7.9 ± 2.3	77.3 ± 5.4	77.1 ± 5.6	66.3 ± 7.2	65.5 ± 7.8	
			20	2.86 ± 0.48	11.4 ± 2.9	66.0 ± 4.1	65.4 ± 5.3	52.9 ± 5.3	52.3 ± 5.2	
		4	5	1.25 ± 0.30	1.6 ± 0.4	96.5 ± 1.6	96.4 ± 1.7	92.2 ± 1.8	91.9 ± 1.9	
			10	1.42 ± 0.38	5.0 ± 1.2	87.7 ± 2.5	87.6 ± 2.5	75.6 ± 5.8	74.8 ± 6.3	
			20	2.69 ± 1.12	10.1 ± 2.8	66.0 ± 5.1	65.8 ± 5.1	53.9 ± 4.7	53.3 ± 4.5	
		8	5	1.03 ± 0.10	3.2 ± 0.3	89.2 ± 1.1	89.0 ± 1.1	82.9 ± 1.2	82.6 ± 1.1	
			10	1.53 ± 0.20	10.8 ± 0.9	72.9 ± 2.7	72.7 ± 2.8	60.5 ± 1.8	59.5 ± 1.5	
			20	2.44 ± 0.27	13.4 ± 2.8	65.0 ± 2.3	64.7 ± 2.2	51.8 ± 2.0	51.2 ± 2.1	
	LM	4	5	1.18 ± 0.14	0.6 ± 0.2	98.4 ± 1.2	97.1 ± 1.2	95.9 ± 1.1	93.3 ± 1.1	8-11
			10	1.52 ± 0.30	1.8 ± 1.0	95.2 ± 2.2	94.3 ± 2.3	90.2 ± 3.9	88.2 ± 3.7	
			20	3.00 ± 0.80	4.5 ± 1.2	86.0 ± 4.1	84.0 ± 4.2	78.8 ± 4.2	75.8 ± 4.4	
10	PM	4	5	1.05 ± 0.10	0.4 ± 0.1	98.4	96.1	96.7	92.0	7-11
			10	1.42 ± 0.10	1.3 ± 0.1	98.0	96.0	93.3	89.1	
			20	2.06 ± 0.12	9.1 ± 0.1	52.8	51.2	42.5	40.1	
	LM	4	5	0.99 ± 0.13	0.2 ± 0.1	98.7	97.1	97.0	94.1	
			10	1.45 ± 0.14	0.3 ± 0.2	94.2	92.5	88.0	84.7	
			20	2.76 ± 0.16	2.7 ± 0.3	91.7	91.3	87.3	86.1	
30	PM	4	5	1.01 ± 0.10	0.3 ± 0.1	96.8	95.5	94.6	92.1	9-11
			10	1.37 ± 0.11	0.7 ± 0.1	97.0	95.5	92.2	88.8	
			20	2.12 ± 0.12	6.3 ± 0.1	76.0	74.1	64.2	60.8	
	LM	4	5	0.85 ± 0.13	0.6 ± 0.1	97.1	95.1	94.2	90.7	
			10	1.54 ± 0.14	0.8 ± 0.2	97.0	95.6	92.6	90.2	
			20	3.14 ± 0.17	1.1 ± 0.3	95.8	94.7	91.2	88.9	

Abbreviations: ROI, regions of interest; IH, inhomogeneity; GPR, gamma passing rate; LM, longitudinal motion; PM, perpendicular motion.
Note. All data are expressed as mean ± SD.
[a] NA, not available.

the moving target provided a dose distribution that was visually similar to that of the stationary target.

The results of the quantitative analysis of the dose distributions are summarized in the Table. For the moving target, varying the period in the range of 2 to 8 seconds did not result in a significant difference in any of the metrics used ($P > .05$), except for the dose in the random pixel within ROI1 (Figure 2a) ($P < .001$). In contrast, varying the peak-to-peak motion resulted in a significant difference in the mean dose in ROI2, the inhomogeneity in ROI1, and the GPR ($P < .001$), except for the mean dose in ROI1 ($P \approx .88$) and the dose in the random pixel within ROI1 ($P \approx .47$). The pixel dose varied unsystematically from 0.81 ± 0.03 (mean ± SD) to 1.19 ± 0.05. Even when the period and peak-to-peak motion were held constant, the pixel dose varied by up to 19% between different irradiations of the moving target.

Both perpendicular and longitudinal motion resulted in dose blurring along the direction of motion, causing the ROI2 dose to increase. For single-fraction irradiation, the ROI2 dose in the moving target increased 2 to 3 times at 20 mm peak-to-peak motion compared to that in the stationary target (Table). The application of multifraction irradiation to the moving target did not reduce the ROI2 dose.

Neither 10 nor 30 fractions had a significant effect ($P \approx .90$). On average, the ROI2 dose was found to be 70% higher for longitudinal motion than that, for perpendicular motion, although no statistically significant difference in the ROI2 dose was observed for either perpendicular or longitudinal motion ($P \approx .57$).

Both perpendicular and longitudinal motion caused an increase in ROI1 inhomogeneity. For single-fraction irradiation, ROI1 inhomogeneity in the moving target increased to 12% ± 3% (mean ± SD) and 4.5% ± 1.2% (Table, Figure 4a) for 20 mm of perpendicular and longitudinal motion, respectively. Perpendicular motion has a greater effect on inhomogeneity than longitudinal motion ($P \approx .003$). Multifraction irradiation with 30 fractions allowed a reduction of ROI1 inhomogeneity to 6.3% ± 0.1% (mean ± SD) and 1.1% ± 0.3% (Table) for 20 mm of perpendicular and longitudinal motion, respectively. A quadratic model was used to fit the experimental inhomogeneity data as a function of the number of fractions (Figure 4c). Agreement between the experimental and fitted data was within 0.1%.

When the moving target was irradiated with a single fraction, the GPR (3%/3 mm) decreased on average down to 65% ± 5% (mean ± SD) and 85% ± 4% (Table, Figure 4b) for 20 mm peak-to-peak perpendicular and longitudinal motion, respectively. For all dose distributions obtained, the mean local GPR was found to be up to 2% lower than the mean global GPR ($P \approx .58$), and the mean 3%/3 mm GPR was 9% higher than the mean 3%/2 mm GPR ($P \approx .001$). Multifraction irradiation with 30 fractions allowed to increase the GPR (3%/3 mm) up to 75.1% and 95.1% (Table) for 20 mm peak-to-peak perpendicular and longitudinal motion, respectively. Figure 5 shows the local gamma index distributions for the 3%/2 mm acceptance criterion for single- and multifraction irradiation at different motion patterns.

For single-fraction irradiation, the threshold for the perpendicular motion was found to be 3 mm, regardless of the acceptance criteria (homogeneity vs 3%/3 mm vs 3%/2 mm) and the calculation method (global vs local). In contrast, for longitudinal motion, it varied from 8 (3%/2 mm, 90%, local) to 11 mm (3%/3 mm, 95%, global), resulting in 10 ± 1 mm (mean ± SD) overall criteria and calculation methods used. For 10-fraction irradiation, the threshold for perpendicular motion ranged from 9 (3%/2 mm, 90%, local) to 11 mm (3%/3 mm, 95%, global). For longitudinal motion, it varied from 7 (3%/2 mm, 90%, local) to 15 mm (homogeneity) with an intermediate value of 11 mm (3%/3 mm, 95%, global). For 30-fraction irradiation, the threshold for perpendicular motion (Figure 4d) varied from 9 (3%/2 mm, 90%, local) to 11 mm (3%/3 mm, 95%, global) with an intermediate value of

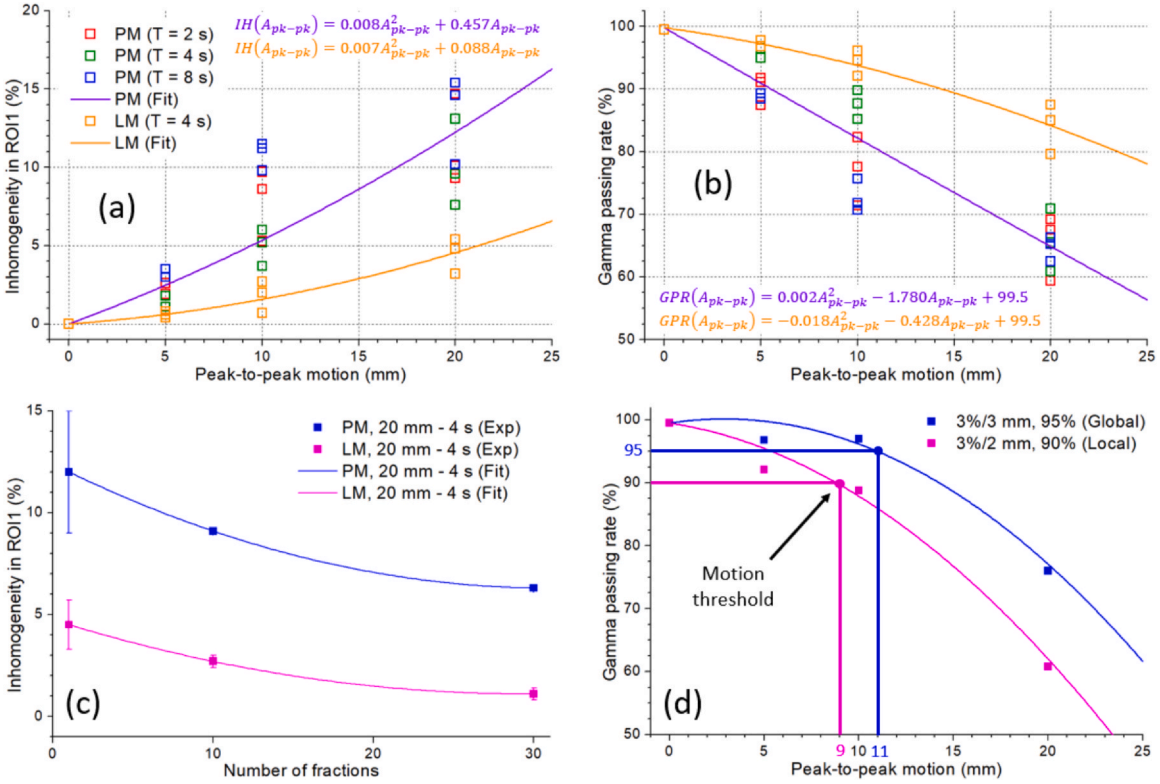

Figure 4. (a) Inhomogeneity in ROI1 and (b) gamma passing rate as a function of peak-to-peak perpendicular motion and longitudinal motion for single-fraction irradiation and different motion periods (T). (c) Inhomogeneity in ROI1 as a function of number of fractions for 20 mm—4 seconds motion pattern. (d) An example of GPR versus peak-to-peak motion curves for the 3%/3 mm and 3%/2 mm acceptance criteria used to calculate the PM threshold for 30-fraction irradiation. In all plots, experimental values and quadratic fit data are indicated by the squares and solid lines, respectively. Abbreviations: GPR, gamma passing rate; IH, inhomogeneity; LM, longitudinal motion; PM, perpendicular motion; and ROI, regions of interest.

10 mm (homogeneity). For longitudinal motion, it was > 15 mm for all criteria and calculation methods used, so only the threshold for perpendicular motion was considered. The calculated motion threshold ranges for different motion types and the number of fractions are shown in the Table.

Discussion

The dose distribution in the moving target was estimated as a function of peak-to-peak motion and period. Peak-to-peak motion range was a dominant parameter affecting all metrics used for both types of motion, except for local dose within the PTV. In contrast, the influence of period variations on all metrics except local dose was found to be insignificant ($P > .05$). The local dose varied by up to 19% for different irradiation sessions. These data confirm the conclusions of Bert et al[9] and Pastor-Serrano et al[7] that variations in period and initial phase significantly influence local dose. Changes in the local dose, when period and peak-to-peak motion were constant, were apparently due to randomization of the initial irradiation phase and variations in the temporal structure of the proton beam delivery.

In addition, when period and peak-to-peak motion were constant, the local dose varied by 19% in different irradiation sessions, apparently due to randomization of the initial irradiation phase and variations in the temporal structure of the proton beam delivery. These considerations confirm the conclusions of Bert et al[9] and Pastor-Serrano et al[7] that variations in period and initial phase significantly influence local dose.

Bert et al[9] reported a root-mean-square homogeneity of 89% for 16 mm peak-to-peak perpendicular motion, while our study found a homogeneity of approximately 88% for similar motion. These results were very similar despite the difference in delivery systems (spot vs raster scanning) and irradiation field size (50 mm × 50 mm vs 110 mm × 110 mm), probably because of a similar motion pattern (perpendicular motion), measurement (EBT3 films), analysis methodology (root-mean-square analysis of dose homogeneity), and beam size ($\sigma \approx 3.5$ mm) were used. In contrast, our result differs from that of Grewal et al[10] who reported a GPR of 96.3% (3%/3 mm, 10% LDT) and 94.1% (3%/2 mm, 10% LDT) for single-fraction irradiation and 10 mm superior-inferior (perpendicular to the beam direction) motion. The GPR in our study was 79% ± 8% (3%/3 mm, 10% LDT) and 67% ± 8% (3%/2 mm, 10% LDT) for similar motion. The difference in results may be primarily due to the larger beam size in Grewal's study than in ours ($\sigma \approx 11.0$ mm vs $\sigma \approx 3.5$ mm).

Protik et al[8] investigated inhomogeneity as a function of peak-to-peak motion along the cranio-caudal direction using 4D simulation based on the 4DCT data sets of lung cancer patients. Dose inhomogeneity was calculated as the standard deviation of the dose difference normalized to the mean PTV dose. The inhomogeneity was reported to be 8% at 20 mm peak-to-peak motion for the 125 cm^3 PTV for the combination of interplay, range, and blur effects. In our study, the inhomogeneity was found to be 12% at 20 mm for a similar PTV. Direct comparison of these results is difficult because there were significant differences in geometry (the simplified water phantom vs the realistic 4DCT-based thoracic geometry) and motion patterns (perpendicular motion only vs a combination of 3 motion effects), delivery parameters (energy switching time, spot delivery time, etc), and beam size ($\sigma \approx 3.1$-3.7 mm vs $\sigma \approx 2.9$-5.6 mm). Despite the differences between these studies, the inhomogeneity as a function of peak-to-peak motion generally followed a quadratic trend in both studies, although the absolute inhomogeneity was different. In addition, in our study, perpendicular motion had a dominant contribution to inhomogeneity compared to WET variations (12.0% vs 4.5%), apparently due to the interplay effect. This is consistent with Protik's study, which showed that the interplay effect introduced a greater dose error than the range effect (7% vs 2.6%).

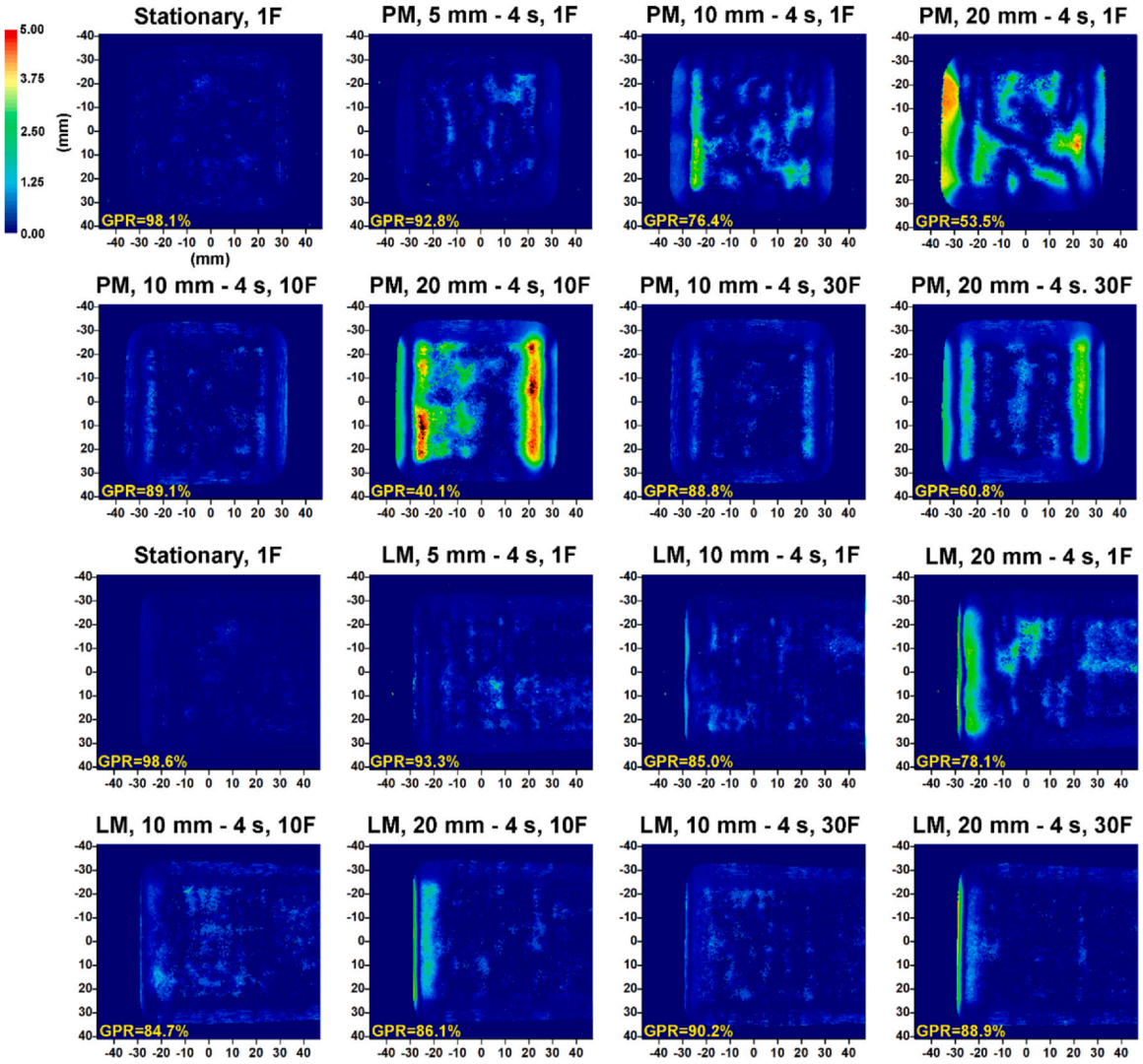

Figure 5. An example of local gamma index distributions with the 3%/2 mm criterion in the stationary target and the moving target irradiated with 1 fraction (1F), 10 fractions (10F), and 30 fractions (30F) at 5 mm—4 seconds, 10 mm—4 seconds, and 20 mm—4 seconds motion patterns during perpendicular motion (beam eye view) and longitudinal motion (side view, beam delivered from the right). These gamma index distributions were calculated for the dose distributions shown in Figure 3. The black color indicates out of range. Abbreviations: GPR, gamma passing rate; LM, longitudinal motion; and PM, perpendicular motion.

In the present study, 5, 10, and 20 mm peak-to-peak target motions were examined. Motion threshold was determined using a quadratic fit curve based on experimental dose homogeneity data and GPR as a function of peak-to-peak motion. Thresholds varied significantly from 3 to 15 mm (Table) depending on the number of fractions (single fraction vs multiple fraction), the type of motion (perpendicular motion vs WET variation), the acceptance criterion (homogeneity vs 3%/3 mm vs 3%/2 mm), and the calculation method (global gamma index vs local) used. For single-fraction irradiation, it was found to be 3 mm, but this value is not clinically relevant because multifield, multifraction irradiation is always used for patient treatment. For multifraction irradiation, our GPR-based motion threshold ranged from 7 to 11 mm for a single field and 10 to 30 fractions. The homogeneity acceptance criterion can also be used to evaluate the motion threshold. On average, it gave almost the same values for perpendicular motion as the GPR-based criterion, which was 10 mm on average. However, the applicability of this criterion is limited because homogeneity characterizes only the dose variance within the high-dose region, but not the low-dose regions beyond the PTV and gradients. In this sense, the calculation of the motion threshold based on GPR seems more preferable. The local gamma index yielded a motion threshold 1 to 2 mm lower than the global gamma index. This may be because the local gamma index highlights errors in low-dose regions and dose gradients, whereas the global gamma index may mask these errors.[26] Motion effects generally distort dose gradients and lead to dose increases in the low-dose regions (see Figure 5), so the local gamma index may be more appropriate for motion threshold assessment.

The present study has several limitations. Simplified geometry and motion patterns were used to simulate target motion. The interplay effect may depend on the tumor location,[6] but the dynamic water phantom used does not allow simulation of different target locations, unlike anthropomorphic phantoms,[27] which have a geometry similar to that of a real patient. In addition, the motion was regular, but real patient breathing patterns are often characterized by irregularities in period and amplitude.[28] This fact may affect the results, because small variations in period can lead to large variations in local dose.[7] Only 1 target volume of 125 cm^3 was used, but the real tumor size varies from tens to hundreds of cubic centimeter and may affect the motion effects.[8] The relationship between target size and motion amplitude may also be important for the interplay effect.[5] The delivered plans included the beams with the energy of 101 to 133 MeV and the size (σ) of 3.1 to 3.5 mm. However, the size (σ) of the beam extracted from the

synchrotron varies in the range of 9.1 to 1.7 mm for the beam energy of 40 to 250 MeV, which may lead to variations in the interplay effect depending on the depth of the tumor. Dose distributions were measured in a single thin central slice of the PTV. At the same time, distortions may be present throughout the target volume and may vary for different isoenergetic slices. When the target moved with WET variations, the radiochromic film was placed parallel to the central axis of the beam. Therefore, the mean dose in ROI2, which was used to evaluate the dose beyond the PTV due to target motion, may be underestimated by up to 20% due to the quenching effect.[24] To minimize this uncertainty, we performed a gamma index analysis by relatively comparing the dose distribution in the moving target with the dose distribution in the stationary target. However, as the target moved, the Bragg peak shifted so that areas of uncertainty due to the quenching effect were not only present in the distal slice of the plane as in the static distribution but also spread along the trajectory of motion, falling into ROI1 and ROI2. This uncertainty cannot be predicted because the moments of beam delivery were randomized relative to the phase of the target motion. This effect limits the accuracy even for relative measurements when studying the influence of WET variations using radiochromic films. In addition, this relative comparison did not take into account the inconsistency between the planned and stationary distributions, so the obtained motion threshold may be slightly overestimated.

Conclusion

Motion effects increased quadratically with increasing peak-to-peak motion, and variations in period only changed the local dose. When the moving target was irradiated with a single fraction, the dose homogeneity deteriorated significantly, and the dose blurred along the direction of motion. The implementation of multifraction irradiation allowed to mitigate hot and cold spots to some extent but did not mitigate dose blurring. The motion threshold for active motion mitigation varied from 7 to 11 mm and depended on the number of fractions, the type of motion, the acceptance criterion, and the calculation method used. The described methodology allowed us to roughly estimate the facility-specific motion threshold. In the future, a careful study of the effects of motion in the 7 to 11 mm range is needed. It is also recommended to introduce separate motion thresholds for different numbers of irradiation fractions depending on whether perpendicular motion or WET variations predominate.

Author contribution

Mikhail Belikhin: Conceptualization, Investigation, Methodology, Formal analysis, Data curation, Visualization, Writing- Original draft. Alexander Shemyakov: Methodology, Validation, Formal analysis, Writing- Review and editing. Alexander Pryanichnikov: Validation, Writing- Original draft, Writing- Review and editing. Alexander Chernyaev: Supervision, Writing- Review and editing.

Declaration of Conflicts of Interest

The authors declare that they have no known competing financial interests or personal relationships that could have appeared to influence the work reported in this paper.

References

1. Kubiak T. Particle therapy of moving targets-the strategies for tumour motion monitoring and moving targets irradiation. *Br J Radiol.* 2016;89(1066):20150275. https://doi.org/10.1259/bjr.20150275
2. Lambert J, Suchowerska N, McKenzie DR, Jackson M. Intrafractional motion during proton beam scanning. *Phys Med Biol.* 2005;50(20):4853–4862.
3. Grassberger C, Dowdell S, Lomax A, et al. Motion interplay as a function of patient parameters and spot size in spot scanning proton therapy for lung cancer. *Int J Radiat Oncol Biol Phys.* 2013;86(2):380–386.
4. Kang M, Huang S, Solberg TD, et al. A study of the beam-specific interplay effect in proton pencil beam scanning delivery in lung cancer. *Acta Oncol.* 2017;56(4):531–540.
5. Kardar L, Li Y, Li X, et al. Evaluation and mitigation of the interplay effects of intensity modulated proton therapy for lung cancer in a clinical setting. *Pract Radiat Oncol.* 2014;4(6):e259–68.
6. Meijers A, Knopf AC, Crijns APG, et al. Evaluation of interplay and organ motion effects by means of 4D dose reconstruction and accumulation. *Radiother Oncol.* 2020;150:268–274.
7. Pastor-Serrano O, Habraken S, Lathouwers D, Hoogeman M, Schaart D, Perkó Z. How should we model and evaluate breathing interplay effects in IMPT? *Phys Med Biol.* 2021;66(23):235003.
8. Protik A, van Herk M, Witte M, Sonke JJ. The impact of breathing amplitude on dose homogeneity in intensity modulated proton therapy. *Phys Imaging Radiat Oncol.* 2017;3:11–16.
9. Bert C, Grözinger SO, Rietzel E. Quantification of interplay effects of scanned particle beams and moving targets. *Phys Med Biol.* 2008;53(9):2253–2265.
10. Grewal HS, Ahmad S, Jin H. Dosimetric study of the interplay effect using three-dimensional motion phantom in proton pencil beam scanning treatment of moving thoracic tumours. *J Radiother Pract.* 2023;22:e11.
11. Lee E, Perry D, Speth J, Zhang Y, Xiao Z, Mascia A. Measurement-based study on characterizing symmetric and asymmetric respiratory motion interplay effect on target dose distribution in the proton pencil beam scanning. *J Appl Clin Med Phys.* 2020;21(4):59–67.
12. Li H, Dong L, Bert C, et al. AAPM Task Group Report 290: respiratory motion management for particle therapy. *Med Phys.* 2022;49(4):e50–e81.
13. Yoshimura T, Shimizu S, Hashimoto T, et al. Analysis of treatment process time for real-time-image gated-spot-scanning proton-beam therapy (RGPT) system. *J Appl Clin Med Phys.* 2020;21(2):38–49.
14. Pryanichnikov AA, Sokunov VV, Shemyakov AE. Some results of the clinical use of the proton therapy complex “Prometheus”. *Phys Part Nucl Lett.* 2018;15(7):981–985.
15. Balakin VE, Alexandrov VA, Bazhan AI, et al. *Status of the proton therapy complex Prometheus. Proceedings of the RuPAC' 18*. JACoW Publishing; 2018:135–138.
16. Balakin VE, Belikhin MA, Pryanichnikov AA, Shemyakov AE, Strelnikova NS. Clinical application of new immobilization system in seated position for proton therapy. *KnE Energy.* 2018;3(2):45.
17. Gordon K, Gulidov I, Semenov A, et al. Proton re-irradiation of unresectable recurrent head and neck cancers. *Rep Pract Oncol Radiother.* 2021;26(2):203–210.
18. Pryanichnikov AA, Chernyaev AP, Belikhin MA, Zhogolev PB, Shemyakov AE, Zavestovskaya IN. Optimization of the low-intensity beam extraction mode at the medical synchrotron for application in proton radiography and tomography. *Mosc Univ Phys Bull.* 2022;77(4):657–660.
19. ProTom Interational. Introducing radiance 330 proton therapy system. Accessed January 28, 2024. https://protominternational.com/introducing-radiance-330–1.
20. P-Cure Ltd. The solution. Accessed January 28, 2024. https://www.p-cure.com.
21. Belikhin MA, Pryanichnikov AA, Chernyaev AP, Shemyakov AE. Nonanthropomorphic dynamic water phantom for spot scanning proton therapy. *Phys At Nucl.* 2022;85(9):1603–1607.
22. Borca VC, Pasquino M, Russo G, et al. Dosimetric characterization and use of GAFCHROMIC EBT3 film for IMRT dose verification. *J Appl Clin Med Phys.* 2013;14(2):158–171.
23. Miften M, Olch A, Mihailidis D, et al. Tolerance limits and methodologies for IMRT measurement-based verification QA: recommendations of AAPM Task Group No. 218. *Med Phys.* 2018;45(4):e53–e83.
24. Khachonkham S, Dreindl R, Heilemann G, et al. Characteristic of EBT-XD and EBT3 radiochromic film dosimetry for photon and proton beams. *Phys Med Biol.* 2018;63(6):065007.
25. Zhao L, Das IJ. Gafchromic EBT film dosimetry in proton beams. *Phys Med Biol.* 2010;55(10):N291–301.
26. Hussein M, Clark CH, Nisbet A. Challenges in calculation of the gamma index in radiotherapy - towards good practice. *Phys Med.* 2017;36:1–11.
27. Colvill E, Krieger M, Bosshard P, et al. Anthropomorphic phantom for deformable lung and liver CT and MR imaging for radiotherapy. *Phys Med Biol.* 2020;65(7):07NT02. https://doi.org/10.1088/1361-6560/ab7508
28. Mutaf YD, Scicutella CJ, Michalski D, et al. A simulation study of irregular respiratory motion and its dosimetric impact on lung tumors. *Phys Med Biol.* 2011;56(3):845–859. https://doi.org/10.1088/0031-9155/56/3/019